JGR Atmospheres

RESEARCH ARTICLE
10.1029/2019JD031010

This article is a companion to Protat et al. (2019), https://doi.org/10.1029/2019JD031011

Key Points:
- The latitudinal variability of statistical oceanic rainfall properties is characterized for the first time
- Results should inform improvements to the GPM radar rainfall retrievals

Correspondence to:
A. Protat,
alain.protat@bom.gov.au

Citation:
Protat, A., Klepp, C., Louf, V., Petersen, W. A., Alexander, S. P., Barros, A., et al (2019). The Latitudinal Variability of Oceanic Rainfall Properties and Its Implication for Satellite Retrievals:1. Drop Size Distribution Properties. *Journal of Geophysical Research: Atmospheres*, *124,* 13,291–13,311. https://doi.org/10.1029/2019JD031010

Received 19 MAY 2019
Accepted 1 OCT 2019
Accepted article online 22 OCT 2019
Published online 14 DEC 2019

The Latitudinal Variability of Oceanic Rainfall Properties and Its Implication for Satellite Retrievals: 1. Drop Size Distribution Properties

Alain Protat[1], Christian Klepp[2], Valentin Louf[3], Walter A. Petersen[4], Simon P. Alexander[5], Ana Barros[6], Jussi Leinonen[7], and Gerald G. Mace[8]

[1]Australian Bureau of Meteorology, Melbourne, Victoria, Australia, [2]Max Planck Institute for Meteorology, Hamburg, Germany, [3]School of Earth, Atmosphere and Environment, Monash University, Melbourne, Victoria, Australia, [4]Earth Science Branch, NASA Marshall Space Flight Center, Huntsville, AL, USA, [5]Australian Antarctic Division, Hobart, Tasmania, Australia, [6]Duke University, Durham, NC, USA, [7]École Polytechnique Fédérale de Lausanne, Lausanne, Switzerland, [8]University of Utah, Salt Lake City, UT, USA

Abstract In this study, we analyze an in situ shipboard global ocean drop size distribution (DSD) 8-year database to understand the underpinning microphysical reasons for discrepancies between satellite oceanic rainfall products at high latitudes reported in the literature. The natural, latitudinal, and convective-stratiform variability of the DSD is found to be large, with a substantially lower drop concentration with diameter smaller than 3 mm in the Southern hemisphere high latitude (S-highlat, south of 45°S) and Northern Hemisphere polar latitude (N-polar, north of 67.5°S) bands, which is where satellite rainfall products most disagree. In contrast, the latitudinal variability of the *normalized* oceanic DSD is small, implying that the functional form of the normalized DSD can be assumed constant and accurately parameterized using proposed fits. The S-highlat and N-polar latitude bands stand out as regions with oceanic rainfall properties different from other latitudes, highlighting fundamental differences in rainfall processes at different latitudes and associated specific challenges for satellite rainfall retrieval techniques. The most salient differences in DSD properties between these two regions and the other latitude bands are: (1) a systematically higher (lower) frequency of occurrence of rainfall rates below (above) 1 mm h^{-1}, (2) much lower drop concentrations, (3) very different values of the DSD shape parameter (μ_0) from what is currently assumed in satellite radar rainfall algorithms, and (4) very different DSD properties in both the convective and stratiform rainfall regimes. Overall, this study provides insights into how DSD assumptions in satellite radar rainfall retrieval techniques could be refined.

1. Introduction

Precipitation is a key source of freshwater. Therefore, observing and monitoring global patterns of precipitation and its intensity and detecting long-term changes in precipitation are critically important for science, society, and understanding our planet in a changing climate. Satellites provide the only platforms from which to measure precipitation globally. In 2014, the National Aeronautics and Space Administration and the Japan Aerospace Exploration Agency launched the Global Precipitation Measurement (GPM) spacecraft. The GPM core satellite carries a dual-frequency Ka/Ku precipitation radar (hereafter DPR) and a multifrequency passive microwave radiometer for measuring the three-dimensional structure of precipitation globally. The GPM core satellite was designed to measure rainfall rates from 0.2 to 110 mm h^{-1} and to detect moderate to intense snow events (Skofronick-Jackson et al., 2017). Understanding precipitation processes and characterizing their variability across different regions of the globe are also a major challenge, as vulnerable communities and farming activities heavily rely on the provision of freshwater to survive.

While the predecessor of GPM, the Tropical Rainfall Measurement Mission (TRMM, e.g., Simpson et al., 1988), focused primarily on the tropical latitudes, the GPM satellite, inclined at ~65°, has allowed the focus to shift to higher latitudes with an emphasis on liquid, mixed phase, and frozen precipitation in middle- and high-latitude weather systems (Skofronick-Jackson et al., 2017). Accordingly, GPM precipitation algorithm developers have worked to modify tropical retrievals originally developed for TRMM in addition to developing new retrievals for converting active and passive measurements from the GPM core observatory into snowfall and rainfall rates in mid- and high-latitude weather systems (Kummerow et al., 2015).

Recent validation efforts of the new GPM algorithms for rainfall rate retrieval have highlighted large statistical discrepancies in zonal precipitation averages between the different operational techniques (dual-frequency only, passive radiometer only, combined radar-radiometer technique, and the Global Precipitation Climatology Project climatology) south of 40°S and north of 40°N in latitude. These systematic differences were first published in Grecu et al. (2016) and Skofronick-Jackson et al. (2017) but are still present in more recent comparisons. Differences of up to a factor 2 are documented in these publications at those high latitudes. Among several possible sources of errors (e.g., different instrument sensitivities, beam filling and rainfall microphysics assumptions, algorithm differences, etc.), incorrect assumptions made about the drop size distribution (DSD) and its variability with latitude in physically based estimation algorithms are expected to play a significant role in differences in statistical rainfall properties between latitude bands. From the global perspective (as opposed to regional, or even continental scale), these validation efforts cannot conclude which satellite products should be trusted, as there is no reference measurement used in these studies on which to base such statement. Beyond these issues with rainfall properties, aerosol-cloud-radiation-precipitation processes over the Southern Ocean region are not correctly represented in global models (e.g., Kay et al., 2016; Trenberth & Fasullo, 2010), which produces substantial biases in absorbed surface shortwave radiation hindering our capability to accurately predict future climate. Producing accurate retrievals of light precipitation properties in this region is therefore critical in that respect as well.

The main objective of this work is to characterize the latitudinal variability of the convective and stratiform oceanic DSD properties using a new in situ shipboard global ocean precipitation database produced by the Ocean Rainfall And Ice-phase precipitation measurement Network (OceanRAIN; Klepp et al., 2018) in order to better understand how rainfall processes differ at different latitudes and better inform future GPM rainfall algorithm developments for the higher latitudes. The OceanRAIN database, briefly described in section 2, was collected using an optical disdrometer specifically designed for all-weather shipboard operations and includes more than 6.83×10^6 min of particle size distribution and fall rate measurements from eight ships, covering select regions at most latitudes from June 2010 to April 2017. Although this data set obviously does not include data from all ocean basins at all latitudes, it is nevertheless an invaluable resource to provide new insights into the latitudinal variability of statistical rainfall properties and new pathways to improving current GPM algorithms for the higher latitudes.

Due to the large number of results to be described, this study is organized in two parts, with Part 1 focusing on the statistical properties, latitudinal variability, and convective-stratiform variability of oceanic DSD properties and associated rainfall obtained with the OceanRAIN database and Part 2 characterizing the latitudinal variability of statistical relationships between radar observables and DSD properties. Both parts provide insights into how current assumptions held in GPM radar rainfall retrieval techniques could be improved over the oceans.

2. The OceanRAIN Database

The OceanRAIN database has been described extensively in Klepp et al. (2018). Here we only briefly provide information relevant to this study. OceanRAIN is a unique in situ global ocean shipboard data set comprising 75 meteorological and oceanographic parameters including precipitation, evaporation, resulting freshwater flux, and surface turbulent fluxes. The precipitation parameters include rain, snow and mixed-phase precipitation occurrence, intensity and accumulation, all derived from particle size distributions measured using automated ODM470 optical disdrometers specifically designed to meet all-weather shipboard requirements (Großklaus, et al. 1998; Klepp, 2015). The ODM470 disdrometer measures particle size in 128 bins between 0.36 and 22 mm, using a logarithmically increasing resolution toward smaller drop sizes, and resulting DSDs are produced at 1-min resolution. Precipitation rates as low as 0.01 mm h^{-1} can be measured by the ODM470, allowing for light precipitation regimes to be examined. These data sets were (and are still being) collected during the long-term installations and special campaigns onboard eight research vessels from June 2010 covering all latitudes (see Figure 1), oceanic basins and seasons and comprise 696,740 precipitation minutes. The high quality of the ODM470 observations in harsh marine environments has been demonstrated in Klepp et al. (2018) using quantitative comparisons between T-matrix calculations of 24 GHz radar reflectivity using the ODM470 DSDs and direct measurements of 24 GHz reflectivity from a micro rain radar

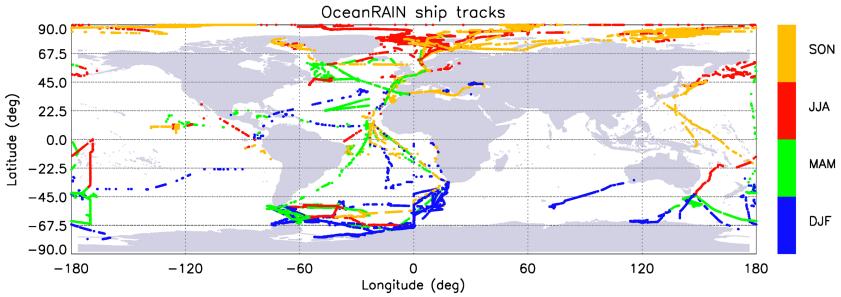

Figure 1. Global map of all Ocean Rainfall And Ice-phase precipitation measurement Network precipitation observations included in this analysis. Colours indicate during which season each observation has been collected. Dashed lines of constant latitude delimit the latitude bins used in this study.

(MRR-2, Klugmann et al., 1996) during the CAPRICORN (Clouds, Aerosols, Precipitation, Radiation, and atmospherIc Composition Over the southeRN ocean) experiment; Mace & Protat, 2018). Correlation between the two estimates was 0.75, with no detectable instrumental artifact at low or high reflectivities. In section 3, we present further validation results using two radar frequencies, which corresponds to two different moments of the DSD. OceanRAIN data are publicly available through the website http://www.oceanrain.org/ and the World Data Center for Climate (data referenced as Klepp et al. 2017a, Klepp et al., 2017b).

The total number of 1-min DSD measurements with precipitation in the OceanRAIN database is 702,641 (about 10% of all measurements including non-rainy minutes). Out of these, 40.7% are classified as snow or mixed phase using an automatic precipitation phase detection algorithm (Burdanowitz et al. 2016) and are therefore discarded from our analysis of rainfall properties. Due to the requirement in our analysis that at least 10 bins are filled with data to produce a fit, 47% of all DSDs are discarded. Due to the rainfall rate being below the ODM470 disdrometer threshold of 0.01 mm h^{-1}, 26.4% are discarded. Note that some DSD measurements can be discarded for multiple reasons among those three. This leaves 18.3% (126,533) of the DSD measurements in the OceanRAIN database validated for our analysis.

3. Methodology

3.1. The DSD Formulation

As demonstrated by the pioneering studies of Testud et al. (2001), Illingworth and Blackman (2002), and Bringi et al. (2002), the DSD can be accurately approximated by a normalized gamma distribution:

$$N(D) = N_0^* \frac{\Gamma(4)\,(3.67+\mu_0)^{4+\mu 0}}{3.67^4\ \Gamma(4+\mu_0)} \left(\frac{D}{D_0}\right)^{\mu_0} exp\left[-(3.67+\mu_0)\frac{D}{D_0}\right] \quad (1)$$

Normalized gamma distributions of rainfall are controlled by three parameters: N_o^* (often called N_w in the literature), the intercept of the distribution; D_0, the median volume diameter of the distribution; and μ_0, the so-called shape parameter of the distribution. In this study, the quality-controlled OceanRAIN DSDs are fitted using this normalized gamma formulation. The three resulting parameters are considered valid only if the DSD has at least 10 size bins filled with data, as recommended in, for example, Jaffrain and Berne (2011) and Tokay et al. (2013).

Thurai and Bringi (2018) recently demonstrated the excellent performance of a generalized gamma model following the double-moment normalization work from Lee et al. (2004), which includes two shape parameters (denoted as μ and c) instead of one in (1). Using moments 3 and 4 of the DSD, the formulation of this generalized gamma fit can be written as:

$$N(D) = N_0^{'}\ c\left[\Gamma\left(\mu+\frac{3}{c}\right)\right]^{-(4+c\mu)}\left[\Gamma\left(\mu+\frac{4}{c}\right)\right]^{(3+c\mu)}\left(\frac{D}{D_m}\right)^{c\mu-1} exp\left[-\left(\frac{\Gamma\left(\mu+\frac{4}{c}\right)}{\Gamma\left(\mu+\frac{3}{c}\right)}\right)^{c}\left(\frac{D}{D_m}\right)^{c}\right], \quad (2)$$

where D_m is the mass-weighted mean diameter (the ratio of the fourth to the third moment of the DSD, e.g., Bringi et al., 2002). Note that D_0 and D_m are related by $D_0/D_m = (3.67+\mu_0)/(4+\mu_0)$, and N_o^* and $N_o^{'}$ are related

by $N_0^*/N_0^{'} = (4^4/6)$. A formulation slightly different from (2) of the double-moment normalization, developed to examine the stability of the functional form of the ice particle size distribution, has been recently proposed in Delanoë et al. (2014):

$$N(D) = N_0^* \ \beta \ \frac{\Gamma(4)}{4^4} \ \frac{\left[\Gamma\left(\frac{\alpha+5}{\beta}\right)\right]^{(4+\alpha)}}{\left[\Gamma\left(\frac{\alpha+4}{\beta}\right)\right]^{(5+\alpha)}} \ \left(\frac{D}{D_m}\right)^{\alpha} \ exp\left[-\left(\frac{\Gamma\left(\frac{\alpha+5}{\beta}\right)}{\Gamma\left(\frac{\alpha+4}{\beta}\right)}\right)^{\beta}\left(\frac{D}{D_m}\right)^{\beta}\right] \tag{3}$$

Formulations (2) and (3) will be used in this study, given the more generalized properties and additional flexibility offered by the generalized gamma fits.

Williams et al. (2014, hereafter referred to as W14) suggested that a lack of statistical independence between the three parameters of the normalized gamma distribution (1) may introduce bias into the TRMM and GPM satellite rainfall rate retrievals. A new framework has therefore been proposed by these authors, based on the two first moments of the mass spectrum: the mass-weighted mean diameter D_m, which is the first moment of the mass spectrum, and σ_m, the standard deviation of the mass spectrum. This σ_m parameter can be calculated directly from D_m and μ_0 as (W14):

$$\sigma_m = D_m/(4+\mu_0)^{1/2} \tag{4}$$

However, as discussed in W14, the two DSD attributes (D_m and σ_m) are not independent, they are in fact highly correlated, as we shall confirm later for different latitude bands and rainfall types. Therefore, a mass spectrum standard deviation σ'_m independent of D_m is obtained using a power-law fit between σ_m and D_m ($\sigma'_m = \sigma_m/{D_m}^{b_m}$), following Haddad et al. (1996). The two statistically independent D_m and σ'_m parameters are then used to build a constraint on μ_0 to reduce the dimension of the radar retrieval problem to two unknowns, ${N_o}^*$ and D_m, using:

$$\mu_0 = \frac{{D_m}^{2-2b_m}}{{\sigma'}_m^2} - 4. \tag{5}$$

Convective-stratiform classification is used in our study to examine the latitudinal variability of DSD properties in convective and stratiform situations separately. Results using a disdrometer-based partitioning technique described by Thurai et al. (2010), which is a simple threshold in the ${N_0}^*$-D_m two-dimensional space derived using a tropical data set, have been compared with using a simple 40-dBZ threshold. Statistical results discussed in what follows were found to be very similar overall. Since the Thurai et al. (2010) technique has been derived from tropical observations only, a simple 40-dBZ threshold has been used to separate convective and stratiform precipitation throughout this study.

3.2. Radar Simulations Using DSDs and Indirect Validation of the DSD Observations

Radar reflectivity Z_H at different frequencies (3 GHz, C-band at 5.6 GHz, Ku-band at 13.6 GHz, Ka band at 35 GHz, and W band at 95 GHz) was estimated from all OceanRAIN DSD measurements using the PyTMatrix code developed by Leinonen (2014), with two objectives in mind: the indirect evaluation of the DSD observations using comparisons with measured radar reflectivities and the development of statistical relationships between radar observables and DSD properties (presented in Part 2). The main assumptions of these T-matrix calculations are the drop shape model and the standard deviation of the drop canting angle (i.e., the angle between the major oblate drop axis and the horizontal axis). In this study, the drop shape model from Thurai et al. (2007) and a standard deviation of the canting angle of 10° are used (settings recommended in pyTMatrix). In this study we will only discuss results obtained at Ku band and Ka band, as these are the two frequencies of the GPM DPR radar.

These T-matrix calculations provide an excellent opportunity to indirectly evaluate the quality of the ODM470 DSD observations, as was done in Klepp et al. (2018) using data from the first phase of the CAPRICORN experiment (Mace & Protat, 2018). During the second phase of the CAPRICORN experiment conducted in January–March 2018 over the Southern Ocean as part of the international Southern Ocean

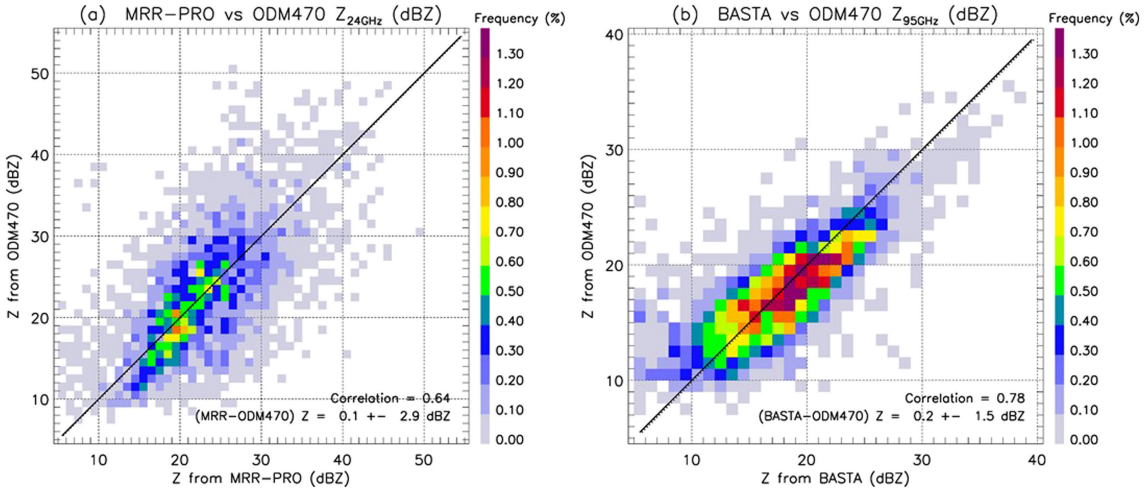

Figure 2. Statistical comparisons of T-matrix calculations of radar reflectivity using drop size distribution measurements and direct reflectivity measurements from (a) the 24 GHz MRR-PRO radar and (b) the 95 GHz BASTA cloud radar. Radar range bins 105 and 100 m above sea level were respectively used for MRR-PRO and BASTA.

Clouds, Radiation, and Aerosol Transport Experimental Study, two vertically pointing radars, the 24 GHz MRR-PRO radar and the 95 GHz BASTA cloud radar (Delanoë et al., 2016), were installed close to the main foremast hosting the ODM470 on *RV Investigator*. Using two radar frequencies allows for two different moments of the DSD to be evaluated independently. Figure 2 shows a good agreement between T-matrix calculations and direct measurements of reflectivity at the two frequencies over a large reflectivity span. Despite very different sampling volumes, differences in height (radar range bins at 105 and 100 m were used for MRR-PRO and BASTA), and inherent errors of the T-matrix calculations (especially at 95 GHz), relatively high correlations of 0.64 and 0.78 are found with MRR-PRO and BASTA, respectively. The most noticeable difference in these comparisons is the slightly lower disdrometer-derived reflectivities relative to MRR-PRO for reflectivities lower than about 15 dBZ. Given that such difference is not observed on the comparisons with the BASTA cloud radar, it is likely that this difference can be attributed to the lack of sensitivity of the MRR-PRO to small drops, rather than a potential problem with the ODM470 disdrometer related to the detection of small drop concentrations. Although these comparisons do not fully characterize the accuracy of number concentration observations in individual bins of the ODM470 disdrometer, they at least demonstrate that integral properties of the DSD are well reproduced by the ODM470 DSDs.

3.3. Latitude Bands for DSD Analysis

To examine the latitudinal variability of DSD properties, we have selected bins for each hemisphere in a way that it broadly discriminates between high-, mid-, sub-, and tropical regimes. These bins are shown as dashed lines on Figure 1. With this latitude band setup, only 146 points were left after validation in our database in the polar band of the Southern Hemisphere (latitude $<-67.5°$S). Therefore, we have not included it in our analysis. Although it does not follow the formal definition of the global regimes, this selection of bands has the advantage of highlighting potential specific differences in DSD properties for latitudes lower than −45° and higher than 45°, which is where satellite rainfall statistics disagree between different satellite products. Let us introduce the terminology and color code used throughout the paper to refer to each latitude band, from the northernmost to the southernmost: N-polar (light blue), N-highlat (dark blue), N-midlat (orange), N-tropics (red), S-tropics (red), S-midlat (orange), and S-highlat (dark blue). The Northern Hemisphere plots will be displayed with solid lines, while the Southern Hemisphere ones will be displayed with dotted lines.

Table 1 shows the total number of samples and percentage of all rainfall samples in each latitude band. The information has also been reported for stratiform and convective rainfall samples separately in Table 1. A large fraction of the rainfall data set has been sampled in the S-highlat band (34% of all samples and 27.6% of the convective samples). The least populated one is the S-tropics band, with only 4.9% of the rainfall

Table 1
Total Number and Percentage of All, Stratiform, and Convective Rainfall Samples in Each Latitude Band

Latitude	S-highlat [−67.5; −45]	S-midlat [−45; −22.5]	S-tropics [−22.5; −0]	N-tropics [0; 22.5]	N-midlat [22.5; 45]	N-highlat [45; 67.5]	N-polar [67.5; 90]
All	42,997	10,836	6,269	17,034	13,715	22,871	12,665
	34.0%	8.6%	4.9%	13.5%	10.8%	18.1%	10.0%
Stratiform	39,343	9,464	5,532	14,159	11,766	20,443	12,440
	34.7%	8.3%	4.9%	12.5%	10.4%	18.0%	11.0%
Convective	3,654	1,372	737	2,875	1,949	2,428	225
	27.6%	10.4%	5.6%	21.7%	14.7%	18.3%	1.7%

Note. Total numbers of samples, stratiform rainfall samples, and convective rainfall samples are 126,533, 113,293, and 13,240, respectively.

samples. Samples are then reasonably evenly distributed among the other latitude bands, which contain 8% to 18.1% of the samples (i.e., about 6,300 to 23,000 individual DSD measurements). Overall, OceanRAIN data have been collected from at least three seasons in all latitude bands except for the N-polar band which only contains JJA and SON data (from the German Polarstern and Maria Merian research vessels, see Figure 2 in Klepp et al., 2018). More year-long data sets in the N-polar band have been collected and will be included in the second release of the OceanRAIN data set. The S-highlat band includes the best balance of rainfall data from all four seasons. In our study, no attempt has been made to further split the data set into seasons as this was resulting in too few samples in too many seasons and latitude bands. It will be very interesting to address this in the future when more data become available. This highlights the need for a sustained long-term program to collect more OceanRAIN observations.

4. The Statistical Properties, Latitudinal Variability and Convective-Stratiform Variability of Rainfall

The overall objective of this section is to analyze the statistical properties and latitudinal variability of the convective and stratiform DSD shapes and associated DSD parameters (N_o^*, D_m, μ_0, σ_m, and σ'_m) and to develop and analyze relationships between rainfall rate and DSD parameters at different latitudes. Results from this section are primarily aimed at better understanding how different rainfall properties are in the higher latitudes and how these differences potentially explain discrepancies between satellite rainfall retrievals at these higher latitudes that predominantly use the same retrieval assumptions at all latitudes.

4.1. DSDs and Normalized DSDs

In this section we document the statistical properties and natural variability of the convective and stratiform DSDs and normalized DSDs and then characterize their latitudinal variability (from our limited number of samples). The underlying motivation is to identify statistical differences which could explain why satellite rainfall retrieval techniques produce very different rainfall statistics at high latitudes.

Figures 3 and 4 show the joint frequency distribution of the DSD $N(D)$ and the normalized DSD $N(D)/N_o^*$, respectively, as obtained from all 1-min DSDs in the OceanRAIN database with more than 10 points and with a rainfall rate higher than the detection threshold of the disdrometer (0.01 mmh^{-1}). As already documented by several authors for DSDs and ice particle size distributions, the natural variability of the DSD is large (Figure 3) but dramatically reduced once scaled by N_o^* (Figure 4). Fits using equations (1), (2), and (3) all approximate very well the normalized DSD. Using the same OceanRAIN database, Duncan et al. (2019) reached the same conclusion. The Thurai and Bringi (2018) and Delanoë et al. (2014) fits provide very similar results and outperform the standard gamma fit (1) for the small normalized diameters. This can be attributed to the more flexible formulation of those fits, boasting one additional fit parameter, as also found and extensively discussed in Thurai and Bringi (2018).

Differences are large between the stratiform (Figure 3b) and convective (Figure 3c) DSDs in our data set, with a general increase in mean drop concentrations for all diameters in convective DSDs, most notably for drop diameters between 1 and 3 mm, and a substantial increase in the frequency of occurrence of diameters greater than 2 mm. In contrast, the normalized concentrations and range of normalized diameters are similar in normalized convective and stratiform DSDs (Figure 4, see also Figure 4a). This result indicates that the

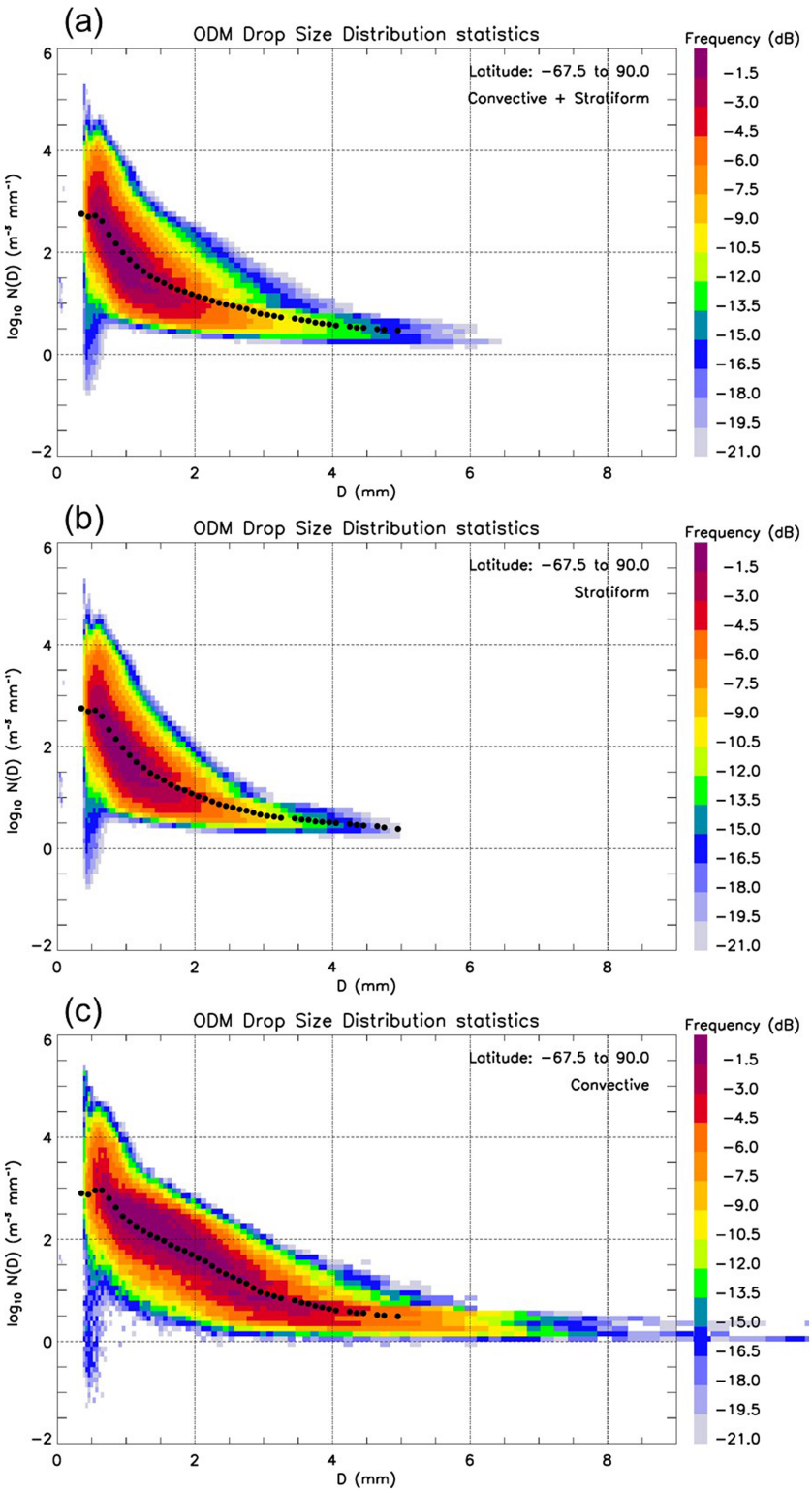

Figure 3. Frequency distribution of the drop size distribution for latitudes between 67.5°S and 90°N, including (a) convective and stratiform samples, (b) stratiform samples only, and (c) convective samples only. Colors show the number of samples in each bin using a logarithmic scale, defined such that the bin with most occurrences has 0 dB and each 50% decrease in occurrence has a 3-dB decrease on the color scale. Black circles show the mean value of drop concentrations in each diameter bin.

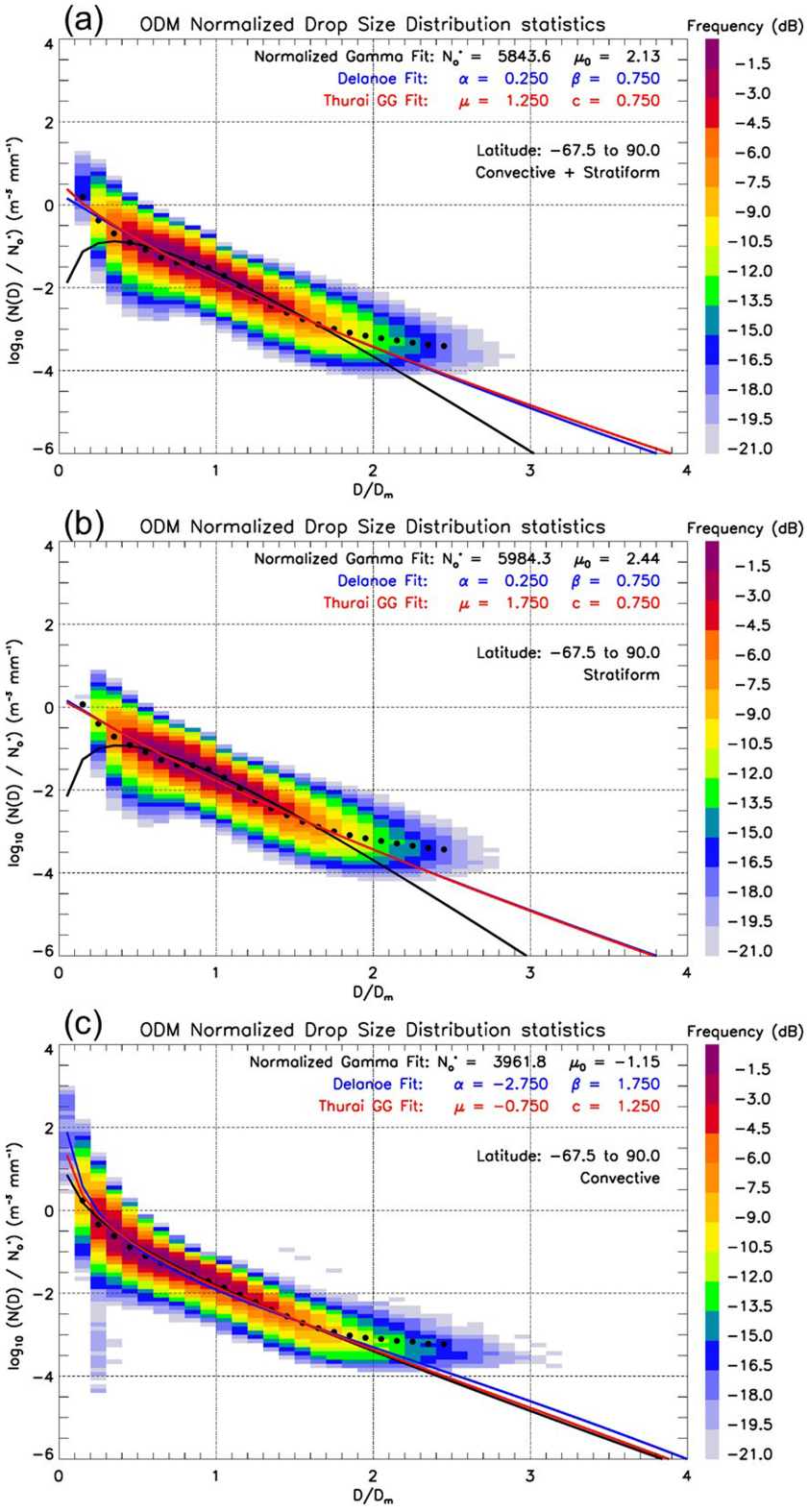

Figure 4. Same as Figure 3 but for the normalized drop size distribution. The black, red, and blue lines are fits derived using equations (1), (2), and (3), respectively. Black circles show the mean value of normalized concentrations in each normalized diameter bin.

convective-stratiform variability is not driven by a change in the functional form of the normalized DSD but by a change in the statistical properties of the DSD parameters used to normalize the distributions (N_o^* and D_m) between the convective and stratiform rainfall regimes. This will be investigated later in this study.

The latitudinal variability of the mean DSD is explored in Figure 5. A substantial latitudinal variability of the mean DSD is found. The midlatitude (orange) mean DSDs are very close to the overall mean throughout the whole range of diameters for both hemispheres. There is a general decrease in drop concentrations with increasing absolute value of latitude. The largest differences in concentration (up to a factor of 4 in our data set) are between the N-tropics and N-polar bands. Tropical mean DSDs (red) are characterized by the highest number concentrations of drops with diameter greater than 1 mm. In the S-highlat (light blue) and N-polar (dark blue) bands, where GPM satellite rainfall products most disagree, the main signature is a substantially lower number concentration of drops with diameter smaller than 3 mm, with a factor 1.9 and 2.4 difference in concentration for $D = 1$ mm with respect to the mean concentration for all DSDs. In Figure 5, we also observe large differences between hemispheres for the high-latitude bands, with the N-highlat concentrations higher (lower) than the S-highlat drop concentrations for drop smaller (bigger) than about 2.2 mm. The lower concentrations of small to medium size drops at high latitudes in the Southern Hemisphere are consistent with the expected indirect effects of much lower aerosol concentrations on cloud formation and resulting rainfall within the pristine Southern Hemisphere air masses at those high latitudes. This result suggests fundamental differences in the efficiency of rainfall microphysical processes and/or substantial aerosol indirect effects on rainfall properties, which cannot be readily addressed with our data set.

It is important to understand how convective and stratiform rainfall regimes contribute to this latitudinal variability in our data set, both from a fundamental rainfall process standpoint, and to provide further insights into satellite rainfall algorithm improvements. As expected, since 90% of the samples are stratiform, the latitudinal variability in stratiform DSDs (Figure 5b) is generally similar to that obtained when all DSDs are included (Figure 5a). However, this variability in stratiform DSDs is markedly lower for all drop diameters, which indicates that both regimes do contribute to the latitudinal variability, despite the much lower frequency of occurrence of convective DSDs (10%). Consistent with this, Figure 5c shows that latitudinal differences in convective rainfall DSDs are indeed substantially larger than for stratiform DSDs (Figure 5b), therefore contributing to the overall latitudinal variability despite the much lower number of convective samples. From our relatively small number of DSD samples in the tropical bands (3,612, see Table 1), we find that tropical convective DSDs are characterized by much higher number concentrations of drops of all diameters. As was the case for stratiform rainfall, there is also a general decrease in number concentrations with increasing absolute value of latitude. As an example, the number concentration of drops with diameter around 2 mm is a factor 2.5 higher in the tropics than in the midlatitude bands concentrations, a factor 3.2 higher than in the high-latitude bands, and a factor 7 higher than in the N-polar latitude band.

In the high-latitude bands, the S-highlat concentrations in convective DSDs are also lower than the N-highlat concentrations for drops smaller than about 2.2 mm (Figure 5c). This statistical signature is therefore driven by both the convective and stratiform rainfall regimes. In contrast, the higher concentration of drops with diameters greater than 2.2 mm in the S-highlat band is driven solely by the convective rainfall regime. This result clearly has implications for satellite radar rainfall algorithm development.

We now turn our attention to the latitudinal variability of the *normalized* DSDs in convective and stratiform regimes (Figure 6). The objective here is to assess whether we can use the same functional form of the normalized DSD for all latitudes and for both convective and stratiform regimes. Figure 6a shows that the latitudinal variability of the mean normalized DSD is much smaller than that of the mean DSD without normalization by N_o^* (Figure 5). The main exception to this general statement is the higher normalized concentrations of normalized diameters in the N-polar band. Luckily, there are no GPM measurements made in that latitude band (GPM measurements are restricted to $\pm 65°$), so no specific adjustment to the functional form of normalized DSDs would be required in GPM rainfall algorithms to account for these higher normalized concentrations in the N-polar band. Going back to our focus on the S-highlat and N-highlat bands, this result clearly suggests from our limited number of samples that specific issues with satellite rainfall statistics at those latitudes cannot be attributed to a fundamentally different functional form of the normalized DSD.

Overall, mean normalized DSDs in convective and stratiform rainfall are similar (Figure 6), with mean normalized drop concentrations similar over the whole normalized diameter range. The main differences are a

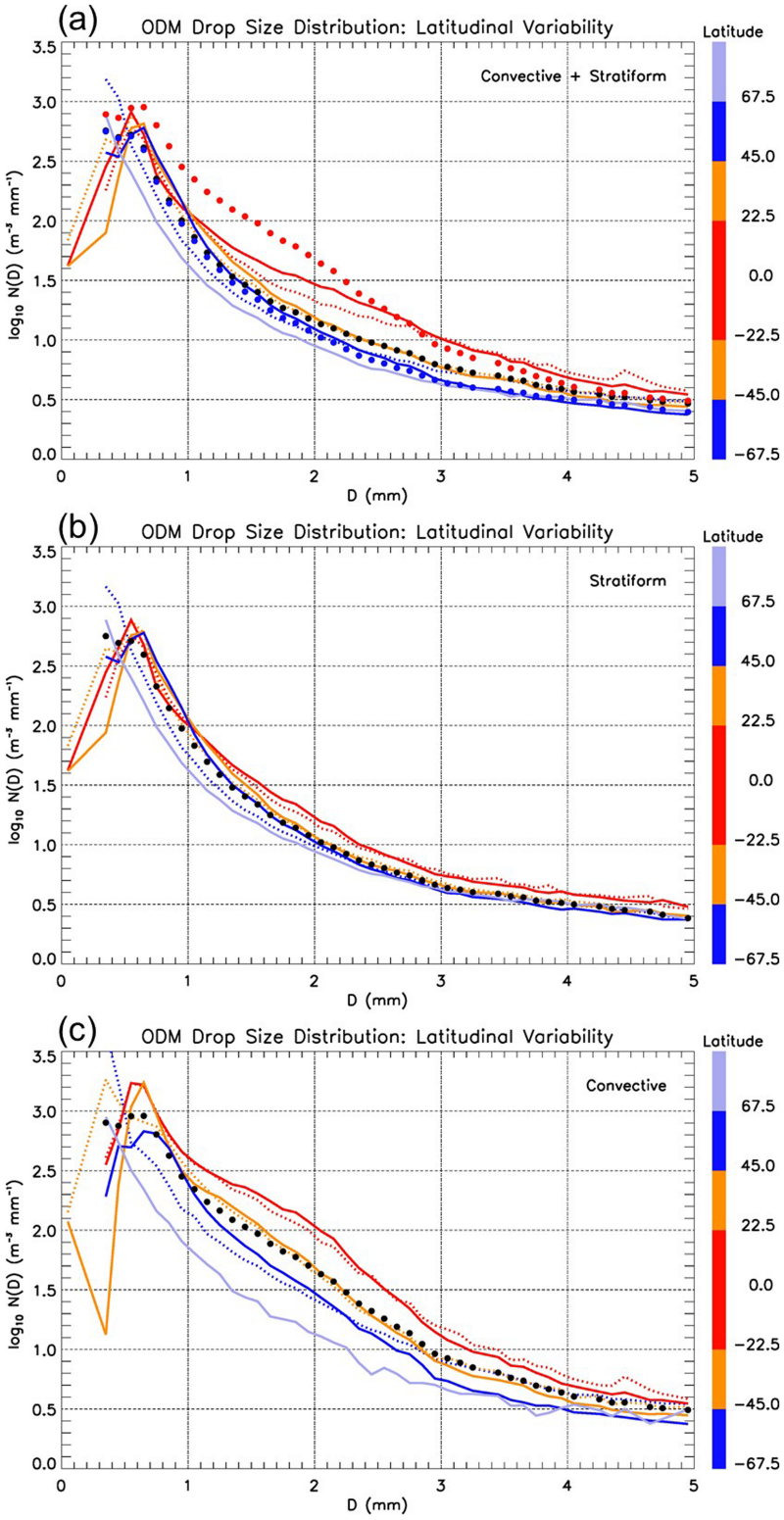

Figure 5. Latitudinal variability of mean drop size distributions (a) for all samples, (b) stratiform samples, and (c) convective samples. Colored lines represent different latitude bands. Solid (dotted) lines are Northern Hemisphere (Southern Hemisphere) results from each latitude band. Black, blue, and red circles in Panel (a) show the mean value of normalized concentrations in each normalized diameter bin for all samples, stratiform samples, and convective samples, respectively. Black circles in Panels (b) and (c) show the mean value of normalized concentrations in each normalized diameter bin for stratiform samples and convective samples, respectively.

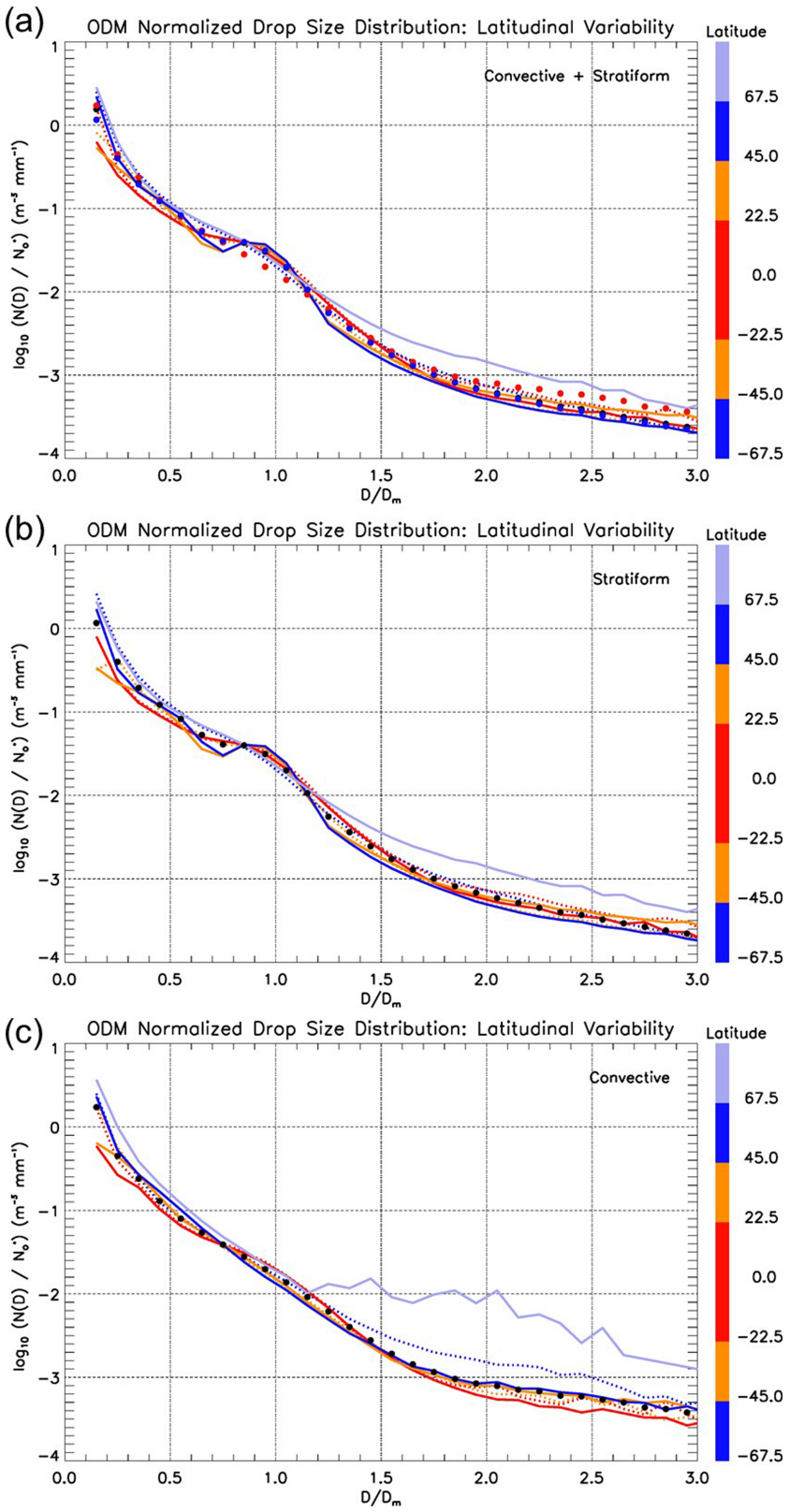

Figure 6. Same as Figure 5 but for mean normalized drop size distributions.

slightly more pronounced "shoulder" in mean normalized stratiform DSDs around normalized diameters of 1 and a slight increase in normalized drop concentration in convective rainfall for $D/D_m > 2$. The other important thing to note from Figure 6 is that the S-highlat band stands out statistically from the other latitude bands in the convective rainfall regime, with higher concentrations of drops with normalized diameters greater than 1.2. However, due to the naturally low frequency of occurrence of convective samples (10% in our database), this important microphysical difference does not produce noticeable statistical differences for the S-highlat band when both the convective and stratiform samples are included (Figure 6a).

The important implication of this small latitudinal and convective-stratiform variability of the functional form of the normalized DSD from a DSD retrieval point of view is that this functional form can be assumed constant (using the two proposed fits, one for convective and one for stratiform) without introducing too much error, leaving two parameters of the normalized DSD to be retrieved (N_o^* and D_m).

4.2. Rainfall Rate and DSD Parameters

The GPM radar rainfall retrieval algorithms (single-frequency and dual-frequency) are currently formulated using the gamma-shaped distribution formalism, which approximates the DSD with three DSD parameters (N_o^*, D_m, and μ_0). Because a major objective of this paper is to characterize the latitudinal variability of rainfall microphysics using DSD measurements to inform further improvements to the GPM algorithms, the focus of this section is to analyze the statistical properties and latitudinal variability of these three DSD parameters. However, new probabilistic GPM rainfall rate retrievals are also under construction as part of the National Aeronautics and Space Administration Precipitation Measurement Missions DSD working group using optimal estimation or Bayesian formulations (based on earlier work from Munchak & Kummerow, 2011; Haddad et al., 2006), which will use the mean and standard deviation of statistically independent DSD attributes (σ'_m and D_m) presented in W14 (see discussion in section 3). The statistical properties and variability of these DSD attributes, and the relationship between these DSD attributes and the gamma DSD parameters, will therefore be explored in our study as well.

The probability distribution function (PDF) of rainfall rate derived from all valid OceanRAIN DSDs is shown as a solid black line in Figure 7a. As expected, the highest frequency of occurrence (2–3%) is found for rainfall rates between 0.5 and 2 mm h^{-1}, and the frequency of occurrence of higher rainfall rates then drops quickly (note the logarithmic scale). The most interesting feature on Figure 7a is the substantial latitudinal variability, which is much larger than the interhemispheric differences in each latitude band. The mean PDF of rainfall rate clearly results from very different contributions from different latitude bands. There is a clear tendency for higher (lower) frequency of occurrence of rainfall rates greater (smaller) than about 1–3 mm h^{-1} with decreasing absolute value of latitude. The N-polar band has no rainfall rate exceeding 10 mm h^{-1} in the OceanRAIN database, and the N-highlat and S-highlat bands have no rainfall rate exceeding 50 mm h^{-1}. In contrast the tropical latitude bands are characterized by a much larger frequency of occurrence of rainfall exceeding 10 mm h^{-1} than the other latitude bands. Going back to our focus on identifying specific differences in rainfall properties in the S-highlat band, Figure 7a clearly shows that the rainfall regime in this pristine environment is noticeably different from the N-highlat band (compare solid and dashed blue lines in Figure 7a), with systematically higher (lower) frequency of occurrence of rainfall rates below (above) 1 mm h^{-1}. It would be interesting (but out of scope of this study) to compare these PDFs with those derived from the GPM radar rainfall retrievals, as was done with the GPM combined algorithm in Duncan et al. (2019) but using our latitude band definitions.

As concluded in the previous section, specific issues with satellite rainfall rate statistics in the high-latitude bands (e.g., Skofronick-Jackson et al., 2017) cannot be attributed to a fundamentally different functional form of the normalized DSD. Therefore, our hypothesis is that these differences result from the latitudinal and/or convective-stratiform variability of some or all of the three DSD parameters (N_o^*, D_m, and μ_0). The PDFs of these DSD parameters and their latitudinal variability are shown in Figures 7b, 7c, and 7d, respectively, for N_o^*, D_m, and μ_0. It appears clearly that the N_o^* and μ_0 parameters are characterized by a high latitudinal variability, while the variability is much smaller for D_m. The S-highlat and N-polar bands clearly stand out in Figure 7b as regions with much lower normalized concentrations N_o^* (N_o^* ~1,400–2,000 compared to a median value for all samples of 5843 in Figure 4a), which is consistent with the much lower drop concentrations for drop diameters lower than 3 mm and the interhemispheric differences at high latitudes

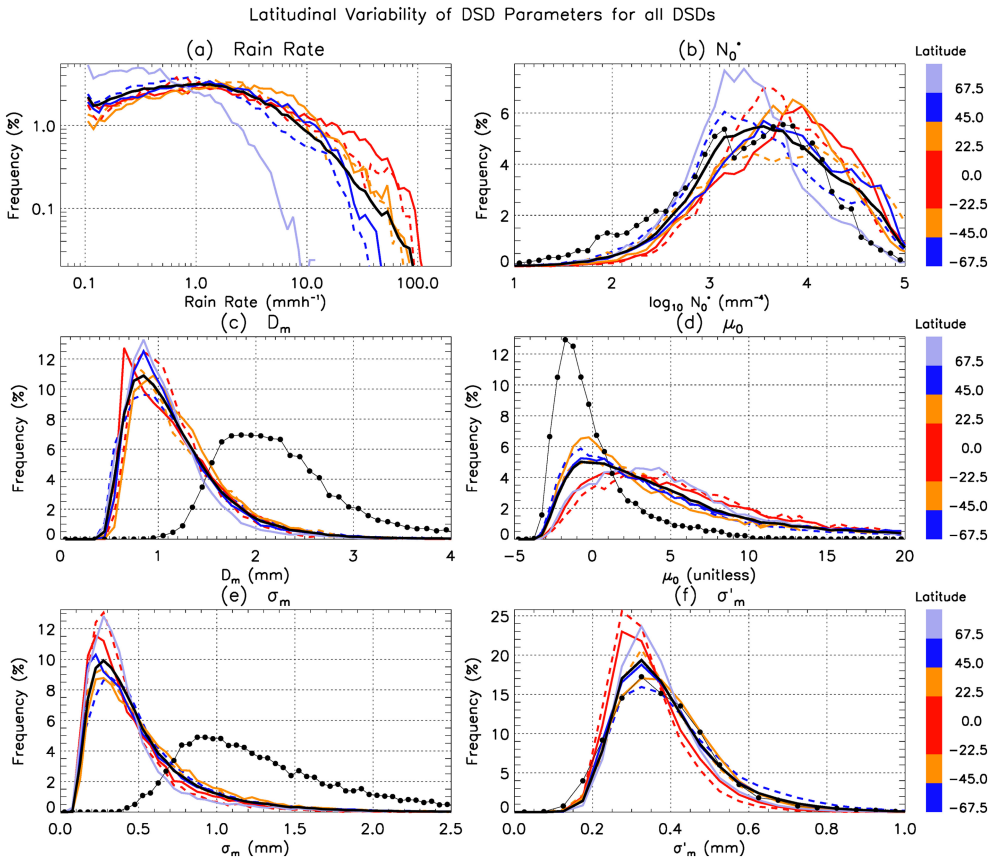

Figure 7. Probability distribution functions of (a) rainfall rate, (b) $log_{10}(N_o^*)$, (c) D_m, (d) μ_0, (e) σ_m, and (f) σ'_m. The black solid line is for all samples, and the coloured lines are for each latitude band (see colour bar). Solid (dotted) lines are Northern Hemisphere (Southern Hemisphere) results from each latitude band. The black circles show the statistics when only convective samples are included. Results using stratiform samples only are not shown as they are nearly undistinguishable from the black line.

(Figure 5). The S-highlat and N-polar PDFs of μ_0 are found to be very different from each other. The high-latitude and midlatitude bands share similar statistical characteristics, with a peak value of μ_0 ranging from −1 to +1. In contrast the N-polar and tropical bands are characterized by much higher peak values of μ_0 ranging from 2 to 5. This finding of large values of μ_0 within the N-polar band is consistent with the analysis of DSD measurements from Finland (Leinonen et al., 2012). Owing to the larger number of samples in the high-latitude and midlatitude bands, the μ_0 distribution obtained by including all samples at all latitudes resembles that of the high-latitude/midlatitude group. This is an important result, since the GPM rainfall algorithms assume either $\mu_0 = 2$ (combined radar–radiometer algorithm, Grecu et al., 2016) or $\mu_0 = 3$ (dual-frequency radar algorithm, Seto et al., 2013). Clearly, these GPM assumptions were inherited from the TRMM era, when algorithms were developed and tuned for the Tropics. Our results clearly suggest that the μ_0 assumption currently held in GPM radar rainfall algorithms needs to be refined to better account for the observed latitudinal variability. Whether such change would in turn positively impact the retrieval of N_o^* for the high latitudes cannot be assessed in the present study. These marked latitudinal variability signatures highlight again some fundamental differences in rainfall properties in the high latitudes of the Southern Hemisphere, consistent with and therefore potentially linked to much lower cloud condensation nuclei and ice nucleating particles concentrations observed within the pristine Southern Hemisphere air masses at those high latitudes (e.g., McCluskey et al., 2018).

The mass spectrum standard deviation parameter, σ_m, (Figure 7e) exhibits a similar level of latitudinal variability as the first moment of the mass spectrum, D_m (Figure. 7c), with similar latitudinal trends. The S-highlat band is characterized by a slightly higher peak value of σ_m (around 0.35) than the N-highlat (around 0.20), tropical (0.20 to 0.25), and midlatitude bands (0.25 to 0.30). Once normalized using the technique

described in W14 and Haddad et al. (1996) to make the normalized mass spectrum standard deviation statistically independent from D_m, the PDF of σ'_m shows a very similar peak value of σ'_m (0.30–0.35) for all latitude bands except in the Tropics (Figure 7f), where the peak value is 0.25–0.30. The other difference is the broader distribution of σ'_m for the S-highlat band, compared to the more peaked distribution in the tropical bands. Overall the latitudinal variability of σ'_m is not large. However, the impact of such variability on probabilistic rainfall retrievals has not been assessed and may not be negligible.

Figure 7 also shows how convective and stratiform rainfall regimes contribute to this latitudinal variability of the DSD parameters (black circles are the PDFs for convective samples only). The stratiform PDFs are not displayed in Figure 7 as they are nearly indistinguishable from the PDFs with all samples included. This shows that most of the latitudinal variability discussed previously comes from the statistical differences in stratiform DSD parameters. The implication of this result from a GPM algorithm perspective is that accounting for the latitudinal variability of the DSD properties for the stratiform rainfall regime, starting with the μ_0 assumption, should have a strong and positive impact on the latitudinal mean statistics of rainfall rate. Figure 7 demonstrates that convective and stratiform regimes are characterized by very different statistical properties of the DSD parameters, which has been documented extensively in the literature since the early work of Tokay and Short (1996) in the Tropics. The largest differences are found for D_m (Figure 7c), μ_0 (Figure 7d), and σ_m (Figure 7e). The peak values of the D_m and σ_m PDFs are more than twice as large for convective rainfall (around 1.8–2.2 and 0.9 mm, respectively, compared to 0.8–0.9 and 0.3 mm in stratiform rainfall). These convective rainfall PDFs of D_m and σ_m are also broader, highlighting the much higher natural variability of rainfall microphysics in the convective regime. In contrast, once σ_m is normalized, the σ'_m PDF is found to be very similar in the convective and stratiform rainfall regimes (Figure 7f), which is an interesting property of rainfall that could be exploited in future GPM probabilistic satellite rainfall retrievals based on the principle of using σ'_m and D_m as statistically independent DSD attributes. The convective μ_0 PDF is also completely different from the stratiform μ_0 PDFs at all latitudes (Figure 7d), with a peak value of -2 to -1.5 and a much smaller standard deviation. Figure 7b also shows that N_o^* distributions are quite similar in convective and stratiform rainfall regimes. This result is *not* consistent with earlier tropical rainfall microphysics studies using DSD measurements (e.g., Testud et al., 2001; Tokay & Short, 1996) or dual-polarization radar retrievals (e.g., Penide et al., 2013), where convective N_o^* is usually larger than stratiform N_o^*. Also, the peak values of the tropical D_m PDF are usually slightly smaller (around 1.6–1.8 mm) than the value reported in Figure 7c (1.8–2.2 mm). One possible explanation for these differences is that the statistical properties presented in Figure. 7 combine very different convective properties from multiple latitudes.

In order to investigate this further, Figure 8 shows the latitudinal variability of the DSD parameters for the convective rainfall regime only. Documenting this latitudinal variability is also extremely important for several applications (including hydrology and extreme rainfall studies) where convective rainfall rates need to be accurately retrieved from space at all latitudes. Although the individual PDFs are noisier due to the smaller number of convective samples in each bin for each latitude, we clearly observe in Figure 8 a substantially higher latitudinal variability of D_m, σ_m, σ'_m, and N_o^* for convective rainfall. Compensating effects coming from different latitude bands are obvious when comparing with the total PDFs (black lines). Peak N_o^* values are much higher in the Tropics than in other latitude bands, and peak values of tropical convective D_m are closer to those found in the literature for the Tropics (1.6–1.8 mm, e.g., Tokay & Short, 1996; Penide et al., 2013). Another important result is how different the N-polar and S-highlat convective DSD properties are compared to other latitudes, highlighting the need for a special treatment of convective rainfall properties in satellite rainfall retrieval techniques. In short, the convective rainfall regime in the N-polar and S-highlat bands is characterized by much smaller N_o^* (Figure 8b) and much larger D_m (Figure 8c) than at other latitudes. Interhemispheric differences in convective properties between the high-latitude bands are also very large, with the S-highlat band characterized by much smaller N_o^* (Figure 8b), much larger D_m (Figure 8c), and much smaller σ'_m (Figure 8f) than the N-highlat band. Although these results are drawn from a limited number of samples and a limited set of associated large-scale conditions, they suggest that these two high-latitude bands cannot be treated in the same way in satellite rainfall algorithms either.

4.3. Relationships Between DSD Parameters and Rainfall Rate

In W14, disdrometer observations collected in Huntsville, Alabama (latitude: 34.7304°N), were used to demonstrate that radar reflectivity, rainfall rate, and σ_m are all correlated with D_m. In this section we

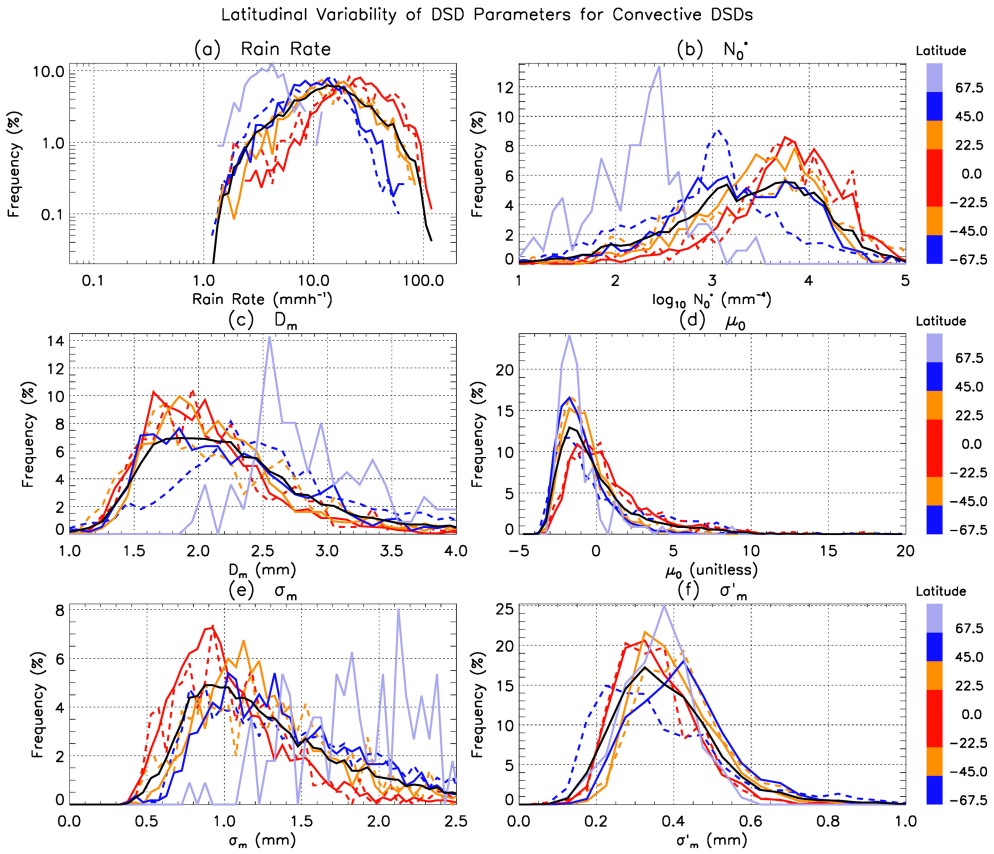

Figure 8. Same as Figure 7 but for convective samples only.

investigate if such correlation is found at all latitudes and how these relationships vary with latitude and with rainfall regime. Developing empirical relationships between DSD parameters for single-frequency or dual-frequency satellite rainfall retrievals requires these DSD parameters to be statistically independent. Figure 9a shows the relationship between σ_m and D_m derived from the OceanRAIN data set. The high correlation already documented for the Huntsville site in W14 is also found with our much larger data set. The all-latitude relationship obtained in our study is nevertheless quite different from that in W14:

$$\sigma_m = 0.349\, D_m{}^{1.531}. \tag{6}$$

The exponent of the relationship, b_m, is higher than the value found in W14 (1.36).

Normalizing σ_m to make it statistically independent from D_m:

$$\sigma'_m = \frac{\sigma_m}{D_m{}^{1.531}} \tag{7}$$

we obtain a higher value of σ'_m than W14 (0.349 versus 0.30). Figure 9d shows the PDF of σ'_m and a Gaussian fit to this PDF, characterized by a mean value $\overline{\sigma'_m} = 0.349$ and a standard deviation std(σ'_m) = 0.100. The Gaussian fit is a good approximation of the σ'_m distribution (which was also the case in W14), albeit some skewness of the σ'_m distribution toward larger values. This implies that σ'_m distributions can be described using Gaussian statistics and can be used in probabilistic rainfall retrieval techniques using $\overline{\sigma'_m}$ and std (σ'_m). As in W14, Figure 9d shows the upper bound ($\overline{\sigma'_m}$ + std(σ'_m) = 0.449) and lower bound ($\overline{\sigma'_m}$ - std (σ'_m) = 0.249) of σ'_m as blue and red dashed lines, respectively, which can in turn be converted using equation (7) to upper and lower bounds for σ_m for each value of D_m. As can be seen in Figure 9a, the W14 relationship falls very close to the lower bound σ_m-D_m relationship derived in our study. The exact same conclusion was also recently reached in a detailed analysis of a 12,177 1-min continental DSD data set (Thurai et al.,

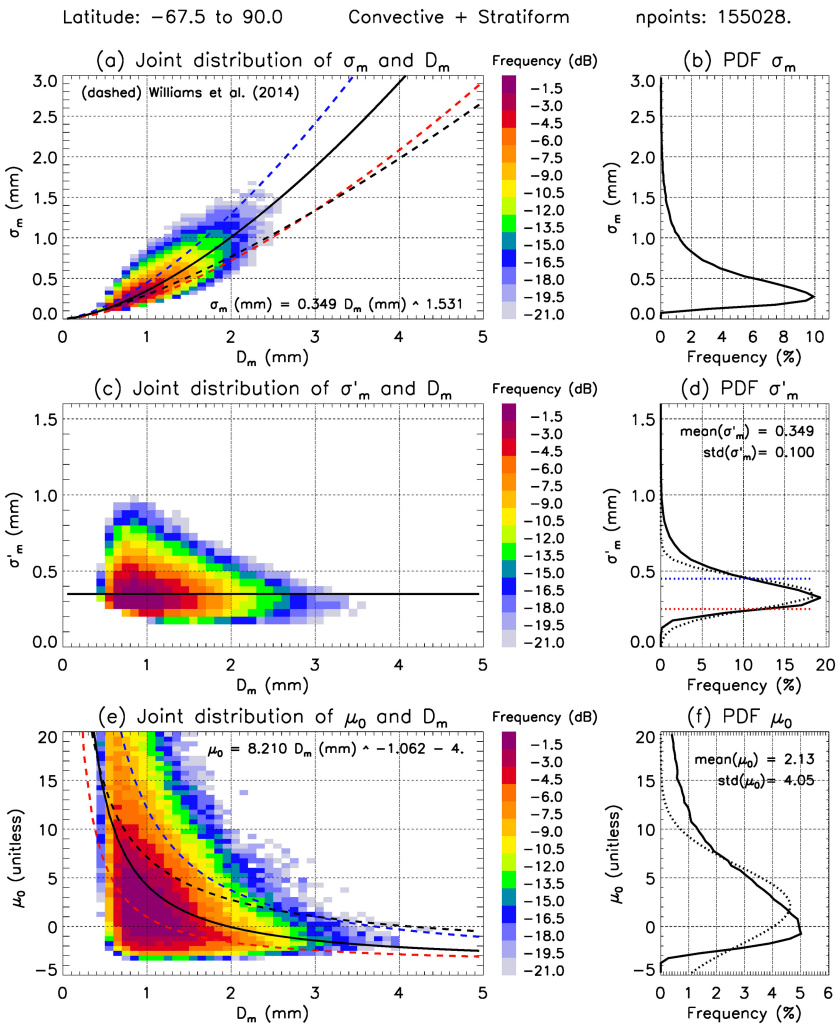

Figure 9. Joint (a) σ_m-D_m, (c) σ'_m-D_m, and (e) μ_0-D_m distributions. Also shown in these panels are power-law fits (solid black lines) and fits derived from one standard deviation more (dashed blue lines) or less (dashed red lines) than the mean value. The dashed black lines are the W14 fits. Panels on the right-hand side are probability distribution functions of (b) σ_m, (d) σ'_m, and (f) μ_0. Dotted lines on panels (d) and (f) are Gaussian fits to the probability distribution functions, with the mean and standard deviation values of these Gaussian fits also reported.

2019). Their σ_m-D_m distribution (Figure 6 in Thurai et al., 2019) is also remarkably similar to that of Figure 9a.

In W14, the statistically independent D_m and σ'_m parameters are used to build a constraint on μ_0 for the satellite rainfall retrieval algorithms. Using this $\mu_0 = f(D_m, \sigma'_m)$ parameterization, W14 suggested that they were able to reduce rainfall retrieval errors (mean and standard deviation) over the whole D_m range compared to using a fixed value of μ_0 ($\mu_0 = 3$ in the GPM DPR retrieval, Seto et al., 2013). Using equation (5) and the results from Figure 9, our general relationship including all latitudes is:

$$\mu_0 = 8.21\, D_m^{-1.06} - 4. \tag{8}$$

Again, the upper and lower bounds of this relationship can be derived from using the upper and lower bounds of σ'_m. These results are reported in Figures 9e and 9f. As also found in W14, the very skewed and wide μ_0 distribution cannot be described accurately using Gaussian statistics, with the median value of the Gaussian distribution ($\mu_0 = 2.1$) largely overestimating the actual peak of the distribution. These results clearly indicate that both the mean and standard deviation of the μ_0 distribution strongly decrease as D_m

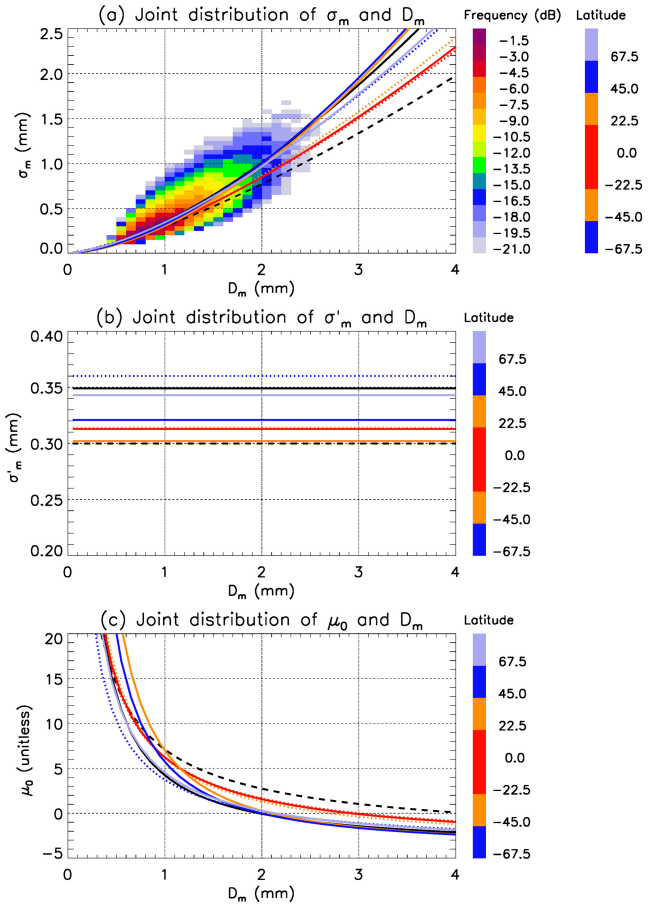

Figure 10. The latitudinal variability of the (a) σ_m-D_m, (b) σ'_m-D_m, and (c) μ_0-D_m joint distributions. Coloured lines are for each latitude band (see colour bar on the right). Solid (dotted) lines are Northern Hemisphere (Southern Hemisphere) results from each latitude band. Also shown in panel (a) is the overall joint histogram of the σ_m-D_m relationship (same as Figure 9a, using the same dB color bar as in Figure 3). The dashed black lines are the W14 fits.

increases. An intriguing difference between the W14 results and our study is that the peak of the μ_0 distribution is around $\mu_0 = 3$ in W14, which is consistent with the assumption in the GPM DPR retrieval technique, while ours is around $\mu_0 = 0$ (Figures 9e and 9f). However, as shown in Figure 7, this mean peak value around μ_0=0 results from compensating effects from different latitude bands, with the tropical bands and the N-polar band distributions peaking around $\mu_0 = 3$ as well.

An important aspect that could not be investigated in W14 is the latitudinal variability of these relationships between DSD parameters. Such study is important to provide optimal constraints to develop GPM rainfall products that account as much as possible for latitudinal and rainfall regime variability. The latitudinal variability of the σ_m-D_m relationship is found to be quite large, especially for $D_m > 1.5$ mm (Figure 10a). The coefficients of all the σ_m-D_m power-law fits are reported in Table 2. The tropical bands and the S-midlat band stand out from the other latitude bands, with systematically lower σ_m as a function of D_m. This difference between fits corresponds to clear shifts of the σ_m-D_m joint distribution (not shown). So, this latitudinal variability explains to some extent the larger standard deviation of the σ_m distribution found in our study compared to the W14 study, where only one location (Huntsville, Alabama) was used.

Once σ_m is normalized to remove its statistical dependence on D_m, a latitudinal variability of σ'_m is still observed (Figure 10b), which implies that probabilistic GPM rainfall algorithms based on the mean and standard deviation of (σ'_m and D_m) should take this latitudinal variability into account. However, it remains to be demonstrated whether such variability (from 0.30 to 0.36) has a measurable effect on these retrievals, which cannot be readily assessed in our study. As has been observed for the individual DSD parameters, the S-highlat and N-polar bands clearly stand out, with higher σ'_m than at other latitudes where σ'_m values range from 0.30 to 0.32. Interhemispheric differences between the N-highlat and S-highlat σ'_m are also found. Interestingly, the N-midlat σ'_m is found to be very close to the W14 value, which was derived in the same latitude band.

As discussed in W14, the statistically independent (σ'_m and D_m) pair can be mapped back onto the gamma DSD parameters to produce a $\mu_0 = \mathrm{f}(D_m$ and $\sigma'_m)$ parameterization for rainfall retrievals assuming gamma distributions. When doing this for each latitude band individually, the different μ_0-D_m fits are found to be quite similar (Figure 10c). Therefore, it seems appropriate to recommend using a single relationship for all latitudes in GPM algorithms to improve upon the $\mu_0 = 3$ assumption. However, further inspection of the joint μ_0-D_m distributions reveals systematic differences between latitude bands (not shown), which could be exploited to refine this assumption at a later stage in collaboration with the GPM algorithm developers.

An important assumption in single-frequency and dual-frequency GPM radar rainfall algorithms is the relationship between rainfall rate (denoted as *R*) and D_m (Iguchi et al., 2017; Kozu et al., 2009). *R*-D_m

Table 2
Coefficients (a_m and b_m) of the $\sigma_m = a_m D_m^{\ b_m}$ Relationship for Each Latitude Band

Latitude	S-highlat [−67.5; −45]	S-midlat [−45; −22.5]	S-tropics [−22.5; −0]	N-tropics [0; 22.5]	N-midlat [22.5; 45]	N-highlat [45; 67.5]	N-polar [67.5; 90]
a_m	0.360	0.314	0.313	0.313	0.302	0.321	0.343
b_m	1.444	1.469	1.426	1.438	1.681	1.684	1.496

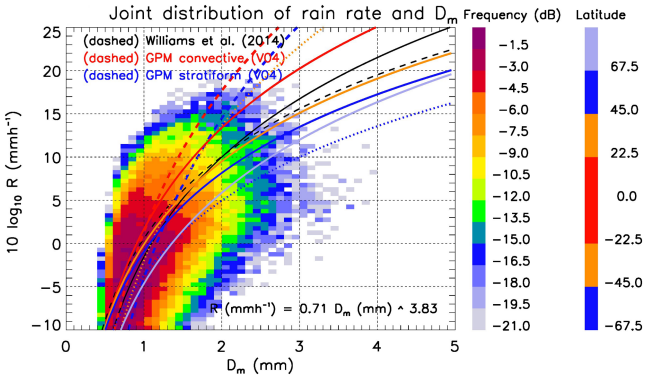

Figure 11. The latitudinal variability of the R-D_m relationship. Coloured solid and dotted lines are for each latitude band (see colour bar on the right). Solid (dotted) lines are Northern Hemisphere (Southern Hemisphere) results from each latitude band. Also shown in color (using the same dB color bar as in Figure 3) is the overall joint R-D_m distribution when all samples are included. The dashed black, red, and blue lines are the W14 fit, Global Precipitation Measurement V04 convective and Global Precipitation Measurement V04 stratiform relationships, respectively.

relationships are assumed for stratiform and convective rain separately to calculate specific attenuation and radar reflectivity for a given rainfall rate at both *Ka* and *Ku* bands. These assumed GPM relationships are:

$$R = 0.401\,\epsilon^{4.649}\,D_m^{\ 6.131} \quad \text{(stratiform)}, \tag{9a}$$

$$R = 1.370\,\epsilon^{4.258}\,D_m^{\ 5.420} \quad \text{(convective)}, \tag{9b}$$

where ϵ is an adjustment factor derived globally from redundant information in the GPM DPR algorithm using path integrated attenuation derived from surface backscatter observations as a 5° × 5° latitude-longitude map in the latest version (V05) of the GPM DPR algorithm. In the earlier version (V04), this adjustment factor was set to $\epsilon = 1$.

Figure 11 shows the joint R-D_m distribution obtained from the OceanRAIN data set when all latitudes are included. Also shown are individual fits obtained within each latitude bin, the W14 relationship, and the GPM V04 relationships (equation (9) with $\epsilon = 1$). The coefficients of all the R-D_m power-law fits are reported in Table 3. The first important result observed in Figure 11 is the large spread of the joint histogram, which implies potentially large errors when using a single relationship at all latitudes. The latitudinal variability of the R-D_m relationship is also found to be large (see different fits in Figure 11 and Table 3), with for instance a factor 2 difference between D_m from the tropical relationships and the S-highlat relationship for R = 10 mm h^{-1} and even more difference for higher rainfall rates. It must be noted however that those higher rainfall rates are much rarer at higher latitudes than in the Tropics, as demonstrated in Figure 7a. Again, the R-D_m relationships obtained in the S-highlat and N-polar bands clearly stand out as being very different from the mean relationship, from the GPM relationships, and from the relationships in other latitude bands. These systematically lower rainfall rates over the D_m range are consistent with the lower number concentrations found in the S-highlat and N-polar bands, since rainfall rate is proportional to N_o^*, while D_m, being a ratio of the fourth to the third moment of the DSD, does not depend on N_o^*.

The second point to note in Figure 11 is the large difference between the mean fit obtained from the OceanRAIN database (solid black line in Figure 11) and the GPM V04 relationships, with much larger Dm for rainfall rates greater than 10 mm h^{-1}. The R-D_m relationship derived including all latitudes is

$$R = 0.710\,D_m^{\ 3.83} \tag{10}$$

This relationship is close to that obtained in W14 but generates lower D_m for very large rainfall rates. As was the case for the σ'_m value, it is interesting to note that the N-midlat R-D_m relationship is very close to that of W14, which had been derived in the same latitude band. The GPM V04 relationships are also found to be in good agreement with our tropical estimates (red lines in Figure 11), which, as was also found for the $\mu_0 = 2$ or 3 assumption (Figure 7), likely reflects the legacy of DSD assumptions from the TRMM era in the GPM rainfall algorithms, when algorithms were developed and tuned for the Tropics.

Table 3
Coefficients (c_m and d_m) of the $R = c_m\,D_m^{\ d_m}$ Relationship for Each Latitude Band, With R in mm h^{-1} and D_m in mm

Latitude	S-highlat [−67.5; −45]	S-midlat [−45;−22.5]	S-tropics [−22.5;−0]	N-tropics [0; 22.5]	N-midlat [22.5; 45]	N-highlat [45; 67.5]	N-polar [67.5; 90]
c_m	0.43	0.64	1.48	1.48	0.98	0.81	0.35
d_m	2.861	5.190	3.885	3.901	3.180	3.018	3.482

5. Summary and Conclusions

The aim of this study was to better understand underpinning microphysical reasons for the large discrepancies between satellite rainfall products at high latitudes over the ocean in the Northern and Southern Hemispheres which are reported in the literature. To do so, we have characterized the latitudinal variability of the convective and stratiform DSD properties and developed and analyzed relationships between radar observables and DSD parameters using a new in situ shipboard global ocean precipitation database produced by the OceanRAIN project (Klepp et al., 2018). Our hope is that these results will inform further GPM rainfall algorithm developments to better account for the observed latitudinal variability in the near future.

We have first analyzed the statistical properties and latitudinal variability of the functional form of all DSDs. We then repeated the same analysis for the convective and stratiform DSDs separately to better understand the contribution of these rainfall regimes to the observed variability. As expected, the natural variability of the DSD is found to be large but dramatically reduced after scaling it by N_o^*. Large differences between stratiform and convective DSDs were also largely reduced after scaling. The latitudinal variability of the mean DSD was found to be substantial, with a general decrease in drop concentrations with increasing absolute value of latitude. In the S-highlat and N-polar bands, where GPM satellite rainfall products most disagree, a substantially lower number concentration of drops with diameter smaller than 3 mm was found. This result highlights fundamental differences in the efficiency of rainfall microphysical processes and/or substantial aerosol indirect effects on rainfall properties. Despite the much larger number of stratiform samples (90%), we find that both the convective and stratiform regimes contribute to this latitudinal variability of the mean DSD. In contrast, the latitudinal variability of the mean *normalized* DSD (and of the normalized convective and stratiform DSDs separately) is much smaller than that of the mean DSD, except for the N-polar band characterized by slightly higher normalized concentrations overall. These results indicate that issues with satellite rainfall rate statistics at high latitudes (e.g., Skofronick-Jackson et al., 2017) cannot be attributed to a fundamentally different functional form of the normalized DSD. From a DSD retrieval standpoint, the important implication of this result is that the functional form of the normalized DSD can be assumed constant and parameterized using the fits proposed in our study, except maybe for the N-polar band where refinements to the normalized DSD formulation may be needed. As was already clearly demonstrated in Thurai et al., (2018) using continental DSD data sets, we also found that general gamma fits, due to their versatility, largely outperform standard gamma fits and should be preferred as the baseline formulation of rainfall retrieval algorithms.

PDFs of rainfall rate and DSD parameters (N_o^*, D_m, μ_0, σ_m, and σ'_m) were then analyzed in different latitude bands to identify differences in rainfall properties within the high-latitude bands. The S-highlat and N-polar bands clearly stood out as regions with systematically higher (lower) frequency of occurrence of rainfall rates below (above) 1 mm h^{-1}, and much lower normalized concentrations N_o^*, which is consistent with (and therefore possibly linked to) much lower cloud condensation nuclei and ice nucleating particles concentrations observed within pristine high-latitude air masses (e.g., McCluskey et al., 2018). Major differences were also found between latitudes for the μ_0 shape parameter, with high-latitude and midlatitude μ_0 ranging from -1 to $+1$ and polar and tropical μ_0 ranging from 2 to 5. This important result clearly suggests that the μ_0 assumption currently held in GPM radar rainfall algorithms needs to be refined to better account for this observed latitudinal variability. Overall the latitudinal variability of D_m, σ_m, and σ'_m was much smaller than that of N_o^* and μ_0. However, the impact of this modest variability on probabilistic rainfall retrievals has not been assessed and may not be negligible.

Splitting the analysis of these PDFs of DSD parameters into the convective and stratiform rainfall regimes shows that convective and stratiform regimes are characterized by very different statistical properties of the DSD parameters, which has been documented extensively in the literature, but more importantly for the purpose of our study that most of the latitudinal variability comes from the statistical differences in *stratiform* DSD parameters between latitudes, due to the much larger number of stratiform samples. The implication of this result from a GPM algorithm perspective is that accounting for the latitudinal variability of the DSD properties for the stratiform rainfall regime, starting with the μ_0 assumption, should have a strong and positive impact on the latitudinal mean statistics of rainfall rate. Although the statistical contribution of the convective regime to the overall latitudinal variability is not as large as that of the stratiform regime, the latitudinal variability of the convective DSD parameters was found to be very large (much large than for

the stratiform regime), with the N-polar and S-highlat convective DSD properties characterized by much smaller N_o^* and much larger D_m than at other latitudes. Interhemispheric differences in convective properties between the high-latitude bands were also very large, with the S-highlat band characterized by much smaller N_o^*, much larger D_m, and much smaller σ'_m than the N-highlat band. This result highlights the need for a special treatment of convective rainfall properties in satellite rainfall retrieval techniques.

In the pioneering work of W14, statistical relationships between DSD parameters and rainfall rate were developed, namely, the σ_m-D_m relationship, the $\mu_0 = \mathrm{f}(D_m, \sigma'_m)$ parameterization and the R-D_m relationship, which are being used in the latest version of the GPM dual-frequency radar technique and for the development of new probabilistic GPM radar rainfall retrieval techniques. The latitudinal variability of these relationships had not been documented, which was therefore the focus of our work. The latitudinal variability of the σ_m-D_m and R-D_m relationships were found to be large, especially for $D_m > 1.5$ mm. Interestingly, our σ_m-D_m distribution derived from all oceanic DSDs from all latitudes was found to be very similar to that derived from a recent analysis of continental DSDs (Thurai et al., 2019), suggesting that land/ocean differences in DSDs might not translate into an large impact on this distribution. In particular, the R-D_m relationships obtained in the S-highlat and N-polar bands clearly stood out as very different from the mean R-D_m relationship when data from all latitudes are included, from the currently assumed GPM relationships, and from the relationships obtained in other latitude bands. Some latitudinal variability of σ'_m was also still observed after normalization of σ_m, which suggests that probabilistic GPM rainfall algorithms based on the mean and standard deviation of (σ'_m, D_m) should probably take this latitudinal variability into account. The μ_0-D_m fits within different latitude bands were quite similar, but further inspection of the joint distributions highlighted systematic differences that could be exploited in GPM algorithms as well.

In Part 2 of this study, we delve into what can be learned from the OceanRAIN data set in terms of relationships between radar observables available from satellite platforms and DSD parameters, how these relationships compare with current GPM radar rainfall algorithm assumptions, how strong the latitudinal variability of these relationships is, and whether this latitudinal variability needs to be included in GPM radar rainfall algorithms. The next natural step of this overall study will be to liaise with GPM algorithm developers and work on introducing the latitudinal variability of statistical rainfall properties where appropriate, then evaluating the resulting statistical improvement in rainfall statistics in the high latitudes using the OceanRAIN database. Due to the difficulty to maintain funding for the OceanRAIN project, we would also like to stress the importance to the scientific community and express our strong support for the continuation of the long-term OceanRAIN sampling.

Acknowledgments
This study was partly funded by the National Environmental Science Program (NESP), Australia. The sustained funding by Initiative Pro Klima (Mabanaft, Mabanaft Deutschland, Petronord and OIL! Tankstellen GmbH & Co. KG) enabled the development, operation and research on OceanRAIN. We greatly appreciate this support and gratefully thank Tanja Thiele, Gerhard Grambow, Volker Tiedemann, Ulrich Freudental and Jan Falke. The project was hosted and co-funded by CliSAP/CEN, University of Hamburg, and the Max Planck Society (MPG). The authors wish to acknowledge the contribution of the Australian Marine National Facility MNF (Brett Muir and Will Ponsonby) for their help setting up and taking care of the ODM470 disdrometer on RV Investigator, and Dr. Toshio Iguchi from the National Institute of Information and Communications Technology, Japan, for useful discussions about details of the GPM dual-frequency radar rainfall algorithm. The Australian Antarctic Division's contribution was supported by project 4387 of the Australian Antarctic program. W. Petersen acknowledges the NASA PMM funding support provided by Dr. G. Skofronick-Jackson and the GPM NASA Ground Validation Program. All OceanRAIN data used in this study are publicly available through the website http://www.oceanrain.org/ and the World Data Center for Climate (WDCC, data referenced as Klepp et al., 2017a, Klepp et al., 2017b).

References

Bringi, V. N., Huang, G., Chandrasekar, V., & Gorgucci, E. (2002). A methodology for estimating the parameters of a gamma raindrop size distribution model from polarimetric radar data: Application to a squall-line event from the TRMM/Brazil Campaign. *Journal of Atmospheric and Oceanic Technology*, *19*(5), 633–645. https://doi.org/10.1175/1520-0426(2002)019<0633:AMFETP>2.0.CO;2

Burdanowitz, J., Klepp, C., & Bakan, S. (2016). An automatic precipitation-phase distinction algorithm for optical disdrometer data over the global ocean. *Atmos. Meas. Tech*, *9*, 1637–1652. https://doi.org/10.5194/amt-9-1637-2016

Delanoë, J., Heymsfield, A., Protat, A., Bansemer, A., & Hogan, R. J. (2014). Normalized particle size distribution for remote sensing application. *Journal of Geophysical Research: Atmospheres*, *119*, 4204–4227. https://doi.org/10.1002/2013JD020700

Delanoë, J., Protat, A., Vinson, J.-P., Brett, W., Caudoux, C., Bertrand, F., et al. (2016). BASTA, a 95 GHz FMCW Doppler radar for cloud and fog studies. *Journal of Atmospheric and Oceanic Technology*, *33*(5), 1023–1038. https://doi.org/10.1175/JTECH-D-15-0104.1

Duncan, D. I., Eriksson, P., Pfreundschuh, S., Klepp, C., & Jones, D. C. (2019). On the distinctiveness of observed oceanic raindrop distributions. *Atmospheric Chemistry and Physics*, *19*(10), 6969–6984. https://doi.org/10.5194/acp-19-6969-2019

Grecu, M., Olson, W. S., Munchak, S. J., Ringerud, S., Liao, L., Haddad, Z. S., et al. (2016). The GPM combined algorithm. *Journal of Atmospheric and Oceanic Technology*, *33*(10), 2225–2245. https://doi.org/10.1175/JTECH-D-16-0019.1

Haddad, Z. S., Durden, S. L., & Im, E. (1996). Parameterizing the raindrop size distribution. *Journal of Applied Meteorology*, *35*(1), 3–13. https://doi.org/10.1175/1520-0450(1996)035<0003:PTRSD>2.0.CO;2

Haddad, Z. S., Meagher, J. P., Durden, S. L., Smith, E. A., & Im, E. (2006). Drop size ambiguities in the retrieval of precipitation profiles from dual-frequency radar measurements. *Journal of the Atmospheric Sciences*, *63*(1), 204–217. https://doi.org/10.1175/JAS3589.1, https://pmm.nasa.gov/sites/default/files/document_files/ATBD_DPR_201708_whole_1.pdf

Iguchi, T., Seto, S., Meneghini, R., Yoshida, N., Awaka, J., Le, M., et al. (2017). GPM/DPR level-2 algorithm theoretical basis document. Retrieved from https://pmm.nasa.gov/sites/default/files/document_files/ATBD_DPR_201708_whole_1.pdf

Illingworth, A. J., & Blackman, T. M. (2002). The need to represent raindrop size spectra as normalized gamma distributions for the interpretation of polarization radar observations. *Journal of Applied Meteorology*, *41*(3), 286–297. https://doi.org/10.1175/1520-0450(2002)041<0286:TNTRRS>2.0.CO;2

Jaffrain, J., & Berne, A. (2011). Experimental quantification of the sampling uncertainty associated with measurements from PARSIVEL disdrometers. *Journal of Hydrometeorology*, *12*(3), 352–370. https://doi.org/10.1175/2010JHM1244.1

Kay, J. E., Wall, C., Yettella, V., Medeiros, B., Hannay, C., Caldwell, P., & Bitz, C. (2016). Global climate impacts of fixing the Southern Ocean shortwave radiation bias in the community earth system model (CESM). *Journal of Climate*, *29*(12), 4617–4636. https://doi.org/10.1175/JCLI-D-15-0358.1

Klepp, C. (2015). The oceanic shipboard precipitation measurement network for surface validation—OceanRAIN. *Atmospheric Research*., Special issue of the International Precipitation Working Group (IPWG), *163*, 74–90. https://doi.org/10.1016/j.atmosres.2014.12.014

Klepp, C., Michel, S., Protat, A., Burdanowitz, J., Albern, N., Dahl, A., et al. (2018). OceanRAIN, a new in-situ shipboard global ocean surface-reference dataset of all water cycle components. *Nature – Scientific Data*, *5*(1). https://doi.org/10.1038/sdata.2018.122

Klepp, C., Michel, S., Protat, A., Burdanowitz, J., Albern, N., Louf, V., et al. (2017b). Ocean rainfall and ice-phase precipitation measurement network—OceanRAIN-R. World Data Center for Climate (WDCC) at DKRZ http://doi.org/10.1594/WDCC/OceanRAIN-R

Klepp, C., Michel, SN. ., Protat, A., Burdanowitz, J., Albern, Louf, V., et al. (2017a). Ocean rainfall and ice-phase precipitation measurement network—OceanRAIN-M. World Data Center for Climate (WDCC) at DKRZ http://doi.org/10.1594/WDCC/OceanRAIN-M

Klugmann, D., Heinsohn, K., & Kirtzel, H. (1996). A low cost 24 GHz FM-CW Doppler radar rain profiler. *Contributions to Atmospheric Physics*, *69*, 247–253.

Kozu, T., Iguchi, T., Shimomai, T., & Kashiwagi, N. (2009). Raindrop size distribution modeling from a statistical rain parameter relation and its application to the TRMM Precipitation Radar rain retrieval algorithm. *Journal of Applied Meteorology and Climatology*, *48*(4), 716–724. https://doi.org/10.1175/2008JAMC1998.1

Kummerow, C., Randel, D. L., Kulie, M., Wang, N.-Y., Ferraro, R., Munchak, S. J., & Petkovic, V. (2015). The evolution of the Goddard profiling algorithm to a fully parametric scheme. *Journal of Atmospheric and Oceanic Technology*, *32*(12), 2265–2280. https://doi.org/10.1175/JTECH-D-15-0039.1

Lee, G. W., Zawadzki, I., Szyrmer, W., Sempere-Torres, D., & Uijlenhoet, R. (2004). A general approach to double-moment normalization of drop size distributions. *Journal of Applied Meteorology*, *43*(2), 264–281. https://doi.org/10.1175/1520-0450(2004)043<0264:AGATDN>2.0.CO;2

Leinonen, J. (2014). High-level interface to T-matrix scattering calculations: Architecture, capabilities and limitations. *Optics Express*, *22*(2), 1655–1660. https://doi.org/10.1364/OE.22.001655

Leinonen, J., Moisseev, D., Leskinen, M., & Petersen, W. A. (2012). A climatology of disdrometer measurements of rainfall in Finland over five years with implications for global radar observations. *Journal of Applied Meteorology and Climatology*, *51*(2), 392–404. https://doi.org/10.1175/JAMC-D-11-056.1

Mace, G. G., & Protat, A. (2018). Clouds over the Southern Ocean as observed from the RV Investigator during CAPRICORN. Part 1: Cloud occurrence and phase partitioning. *Journal of Applied Meteorology and Climatology*, *57*(8), 1783–1803. https://doi.org/10.1175/JAMC-D-17-0194.1

McCluskey, C. S., Hill, T. C. J., Humphries, R. S., Rauker, A.-M., Moreau, S., Strutton, P. G., et al. (2018). Observations of ice nucleating particles over Southern Ocean waters. *Geophysical Research Letters*, *45*(21), 11,989–11,997. https://doi.org/10.1029/2018GL079981

Munchak, S. P., & Kummerow, C. D. (2011). A modular optimal estimation method for combined radar-radiometer precipitation profiling. *Journal of Applied Meteorology and Climatology*, *50*(2), 433–448. https://doi.org/10.1175/2010JAMC2535.1

Penide, G., Kumar, V., Protat, A., & May, P. T. (2013). Statistics of drop size distribution parameters and rain rates for stratiform and convective precipitation during the North-Australian wet season. *Monthly Weather Review*, *141*(9), 3222–3237. https://doi.org/10.1175/MWR-D-12-00262.1

Seto, S., Iguchi, T., & Oki, T. (2013). The basic performance of a precipitation retrieval algorithm for the Global Precipitation Measurement Mission's single/dual-frequency radar measurements. *IEEE Transactions on Geoscience and Remote Sensing*, *51*(12), 5239–5251. https://doi.org/10.1109/TGRS.2012.2231686

Simpson, J. R., Adler, R. F., & North, G. R. (1988). A proposed Tropical Rainfall Measuring Mission (TRMM) satellite. *Bulletin of the American meteorological Society*, *69*(3), 278–295. https://doi.org/10.1175/1520-0477(1988)069<0278:APTRMM>2.0.CO;2

Skofronick-Jackson, G., Petersen, W. A., Berg, W., Kidd, C., Stocker, E. F., Kirschbaum, D. B., et al. (2017). The Global Precipitation Measurement (GPM) mission for science and society. *Bulletin of the American meteorological Society*, *98*(8), 1679–1695. https://doi.org/10.1175/BAMS-D-15-00306.1

Testud, J., Oury, S., Black, R. A., Amayec, P., & Dou, X. K. (2001). The concept of "normalized" distribution to describe raindrop spectra: A tool for cloud physics and cloud remote sensing. *Journal of Applied Meteorology*, *40*(6), 1118–1140. https://doi.org/10.1175/1520-0450(2001)040<1118:TCONDT>2.0.CO;2

Thurai, M., Bringi, V., Gatlin, P. N., Petersen, W. A., & Wingo, M. T. (2019). Measurements and modeling of the full rain drop size distribution. *Atmosphere*, *2019*(10), 39.

Thurai, M., & Bringi, V. N. (2018). Application of the generalized gamma model to represent the full rain drop size distribution spectra. *Journal of Applied Meteorology and Climatology*, *57*(5), 1197–1210. https://doi.org/10.1175/jamc-d-17-0235.1

Thurai, M., V. N. Bringi, , and P. T. May, 2010: CPOL radar-derived drop size distribution statistics of stratiform and convective rain for two regimes in Darwin, Australia. *Journal of Atmospheric and Oceanic Technology*, *27***(5)**, 932-942, DOI: https://doi.org/10.1175/2010JTECHA1349.1.

Thurai, M., Huang, G. J., Bringi, V. N., Randeu, W. L., & Schönhuber, M. (2007). Drop shapes, model comparisons, and calculations of polarimetric radar parameters in rain. *Journal of Atmospheric and Oceanic Technology*, *24*(6), 1019–1032. https://doi.org/10.1175/JTECH2051.1

Tokay, A., Petersen, W. A., Gatlin, P., & Wingo, M. (2013). Comparison of raindrop size distribution measurements by collocated disdrometers. *Journal of Atmospheric and Oceanic Technology*, *30*(8), 1672–1690. https://doi.org/10.1175/JTECH-D-12-00163.1

Tokay, A., & Short, D. A. (1996). Evidence from tropical raindrop spectra of the origin of rain from stratiform versus convective clouds. *Journal of Applied Meteorology*, *35*(3), 355–371. https://doi.org/10.1175/1520-0450(1996)035<0355:EFTRSO>2.0.CO;2

Trenberth, K. E., & Fasullo, J. T. (2010). Simulation of present-day and twenty-first-century energy budgets of the southern oceans. *Journal of Climate*, *23*(2), 440–454. https://doi.org/10.1175/2009JCLI3152.1

Williams, C. R., Bringi, V. N., Carey, L. D., Chandrasekar, V., Gatlin, P., Haddad, Z., et al. (2014). Describing the shape of raindrop size distributions using uncorrelated raindrop mass spectrum parameters. *Journal of Applied Meteorology and Climatology*, *53*(5), 1282–1296. https://doi.org/10.1175/JAMC-D-13-076.1